Gasified Rice Husk Porous Carbon Loaded S-doped Tin Oxide Composite for Supercapacitor Electrode

Huilin Wang,[a,b,c] Dajun Wu,[b] Jianbin Zhou,[a,*] and Gang Yang [b,*]

Gasified rice husk carbon, which is a byproduct of power generation by gasification, can be converted to porous carbon (RHAC). This product is environmentally friendly, has excellent electrochemical performance, and represents a high value utilization of biomass resources. In this paper, the heterostructured nano composites were synthesized by a simple hydrothermal reaction. RHAC loaded sulfur-doped tin oxide was used to synthesize composites with a highly conductive porous structure, short ion/electron transport path, and enhanced pseudo capacitance kinetics. The specific capacitance of this composite was improved over that of biomass porous carbon RHAC. At a current density of 1.5 A/g, the specific capacitance of S-doped RHAC/SnO$_2$ composite, RHAC/SnO$_2$ composite, and RHAC were 215 F/g, 177 F/g, and 141 F/g, respectively. The current density was increased from 1 A/g to 5 A/g, and the specific capacity of the S-doped RHAC/SnO$_2$ composite was maintained at 67% with good rate performance. At a current density of 0.4 A/g, the charge capacity was maintained at 78.5% after 5000 cycles of charge and discharge, indicating that the electrode has a long cycle life.

Contact information: a: College of Materials Science and Engineering, Nanjing Forestry University, Nanjing 210037, China; b: Changshu Institute of Technology, Changshu 215500, China; c: Suzhou Agricultural Modernization Research Center, Changshu 215500, China;
* Corresponding author: whl@cslg.edu.cn

INTRODUCTION

Mankind has entered a period of conflict between energy supply and demand, hence the use of green and renewable energy has become an inevitable trend of sustainable development. The exploitation of biomass energy is a very effective solution. Biomass sources have a large production volume, and the comprehensive utilization efficiency is relatively low. There has been much research on the development and utilization of biomass energy. The application of biomass-based carbon materials in the field of supercapacitors has become a research hotspot in the field of biomass resource utilization in recent years. The internal structure of biomass resources based on agricultural and forestry wastes makes it an ideal precursor for the production of porous carbon for the application to supercapacitor electrode materials (He *et al.* 2013; Chen *et al.* 2017; Tang *et al.* 2017). Supercapacitors are widely used as promising energy storage devices with the advantages of short charging time, high power density, and long cycle life (Lang *et al.* 2011). The performance of supercapacitors is closely related to electrode materials. Carbon materials have the advantages of good stability, low cost, long cycle life, and high specific power, but their energy density is relatively low (Lang *et al.* 2011; Kim *et al.* 2016).

Metal oxides undergo a reversible redox reaction that provides pseudo-capacitance, which increases the specific capacitance and specific energy of the electrode material (Zhou *et al.* 2013a; Chuanxiang *et al.* 2016; Huang *et al.* 2016). SnO_2 is a semiconductor material with abundant raw materials, low cost, high electrochemical activity, high power density, and environmental friendliness (Jin *et al.* 2011; Jiang *et al.* 2012). It forms rich nanostructures (Wang and Rogach 2014) and has been widely used in lithium ion batteries (Joshi *et al.* 2016; Ma *et al.* 2016; Madian *et al.* 2016; Peng *et al.* 2016; Xia *et al.* 2016). However, SnO_2 has strong polarity, and therefore, SnO_2 particles are prone to agglomeration, hindering the insertion and extraction of electrolyte ions, and low electrochemical utilization, which limits its application in supercapacitors (Lim *et al.* 2012; Deosarkar *et al.* 2013). When tin dioxide is compounded with other materials such as metal oxides (Zhou *et al.* 2018) and carbon-based materials (Li *et al.* 2012; Lim *et al.* 2013), the composite electrode combines the advantages of these materials, which is an effective method for improving the electrochemical performance of tin dioxide. Composites with high specific surface area and porosity are used to improve the defects of SnO_2 structures (Hwang and Hyun 2007). SnO_2 composites are prepared by different methods and applied to supercapacitor electrode materials. Hwang and Hyun (2007) impregnated the $SnCl_4$ solution into the carbon aerogel electrode to obtain a SnO_2/carbon aerogel composite, which is calculated by constant current charge and discharge method. The specific capacitance is 69.8 F/g at a current density of 10 mA/g. Rakhi *et al*. (2012) used a chemical method to load SnO_2 on graphene nanosheets, where the specific capacitance of SnO_2/graphene nanosheets was 195 F/g. Mu *et al*. (2011) made a heterostructure of SnO_2/carbon nanofibers by electrospinning and template solvothermal method. The maximum specific capacitance of the composite sample was 187 F/g at a scan rate of 20 mV/s. Li *et al*. (2012) synthesized the SnO_2/SWCNTs core-shell nanowires by electrodeposition technology with higher specific capacitance 320 F/g, at the scanning rate of 6 mV/s.

Although the above SnO_2/carbon composites have high electrochemical performance, the preparation of expensive carbon-based materials and the complicated techniques for synthesizing composites hinder their industrial application. In this paper, based on the preparation of porous carbon (RHAC) from gasification power generation by-product gasified rice husk carbon, the composite of RHAC loaded SnO_2 was further studied as a supercapacitor electrode. The S-doped micro-mesoporous SnO_2/RHAC composites were synthesized by a simple hydrothermal method and used to prepare supercapacitor electrode materials. The *in situ* synthesis method is simple, with low costs, and the electrochemical performance of the electrodes is excellent.

EXPERIMENTAL

Materials

RHAC was prepared from the byproduct of rice husk gasification power generation boiled with KOH solution and activated by CO_2, as previously described (Wang *et al.* 2018). $SnCl_2 \cdot 2H_2O$, ethanediamine, CH_4N_2S, Ni foam, and absolute ethanol were obtained from Shanghai Sinopharm Chemical Co., Ltd. of Shanghai, China.

Methods

For the preparation of S-doped RHAC/SnO_2 composites, 1 mmol $SnCl_2 \cdot 2H_2O$ and

2 mmol of NH_2CSNH_2 were dissolved in 30 mL of deionized (DI) water; 120 mg of RHAC was dissolved in 30 mL of deionized (DI) water by ultrasonication for 10 min and then added into the $SnCl_2$ solution with continuous stirring. After stirring at room temperature for 2 h, the mixture was transferred into a Teflon-lined stainless steel autoclave. The sealed autoclave was kept at 160 °C for 12 h in an oven and then cooled to room temperature. The products were washed with DI water and absolute ethanol three times and finally dried in a vacuum oven at 70 °C. The product was annealed in N_2 atmosphere at 400 °C for 2 h. For comparison, the $RHAC/SnO_2$ composite was synthesized by the solvothermal method without NH_2CSNH_2, 1 mmol $SnCl_2 \cdot 2H_2O$ and 270 µL of ethanediamine were dissolved in 30 mL of glycol, and 120 mg of RHAC was dissolved in 30 mL of deionized (DI) water.

Characterization

The pore structure parameters of porous carbon were analyzed by Q10 automatic analyzer (Quantachrome Corporation, Boynton Beach, FL, USA). Using nitrogen gas as an adsorbent, the absorption/desorption experiment was performed at 77 K. The specific surface area was calculated by the Brunauer-Emmett-Teller (BET) method, and the distribution was calculated by the density functional theory (DFT) method. The morphology of the product was analyzed by scanning electron microscopy (JSM-7600F, JEOL, Tokyo, Japan) and transmission electron microscopy (TEM, JEM-2100F, JEOL). The structure and phase of the sample were analyzed by X-ray powder diffraction (XRD; D/Max-2200/PC, Rigaku, Tokyo, Japan), and scanning was performed at a speed of 5 °/min and a range of 2 to 80°. X-ray photoelectron spectroscopy (XPS, escalab250xi, Thermo Scientific, Waltham, MA, USA) was used to study the surface chemical state of porous carbon composites, while the Gaussian function and Lorentz function were used to fit the curve for XPS analysis.

Electrochemical Measurements

The foamed nickel was cut into a size of 1 cm × 2 cm. It was ultrasonicated in acetone solution, 0.5 M HCl solution, deionized water, and ethanol for 15 min, respectively, to wash the surface oil impurities and oxide film. It was then dried in a vacuum drying oven. The prepared composite material was mixed with acetylene black and polytetrafluoroethylene according to a mass ratio of 8:1:1, and N- Methylpyrrolidone (NMP) was used as a solvent. The above mixture was stirred into a well-mixed slurry, then uniformly coated on a foamed nickel collector, dried in a vacuum oven at 80 °C for 12 h, and removed at room temperature. Tableting was carried out at a pressure of 10 MPa. The working electrode area was 1 cm x 1 cm, and the mass loading of the electrode material was approximately 4 mg. The traditional three-electrode test was carried out in the electrochemical workstation (Chenhua, Shanghai, China) containing 6.0 M KOH aqueous solution as the electrolyte. The S-doped $RHAC/SnO_2$ composite, $RHAC/SnO_2$ composite, and RHAC electrodes were used as the working electrode, respectively, and a standard calomel electrode (SCE) was used as the reference electrode and the platinum plate as counter electrode. The cyclic voltammetry (CV), constant current charge and discharge (GCD) and AC impedance (EIS) tests were performed. The mass specific capacitance at different charge and discharge current densities was determined according to Eq. 1,

$$C = I \cdot t / (m \cdot \Delta V) \tag{1}$$

bioresources.com

where C is the specific capacitance (F/g), I is the discharge current (A), t is the discharge time (s), m is the mass of the active materials in the single electrode (g), and ΔV is the potential difference (V) in the discharge process.

RESULTS AND DISCUSSION

Morphology and Structure Analysis of RHAC/SnO₂ and S-doped RHAC/SnO₂

The XRD pattern of the composite material is shown in Fig. 1. It can be seen that the composite material of RHAC/SnO$_2$ and the S-doped RHAC/SnO$_2$ heterostructure composite obtained by hydrothermal reaction. Excluding the C(002) and C(100) diffraction peaks from RHAC, the XRD pattern of RHAC/SnO$_2$ consisted of SnO$_2$ and a small amount of SnO. Both RHAC/SnO$_2$ and S-doped RHAC/SnO$_2$ composites had significant SnO$_2$ characteristic diffraction peaks at 2θ = 26.6°, 33.9°, 51.8°, 65.9°, 71.3°, and 78.7° (JCPDS No. 41-1445). In addition, there were distinct S-signal diffraction peaks at 2θ = 33.8°, 38.8°, 43.7°, and 70.8° (JCPDS No. 20-1225) in S-doped composites. The broad peak indicated the low crystal structure of SnO$_2$ in the S-doped RHAC/SnO$_2$ nanocomposite.
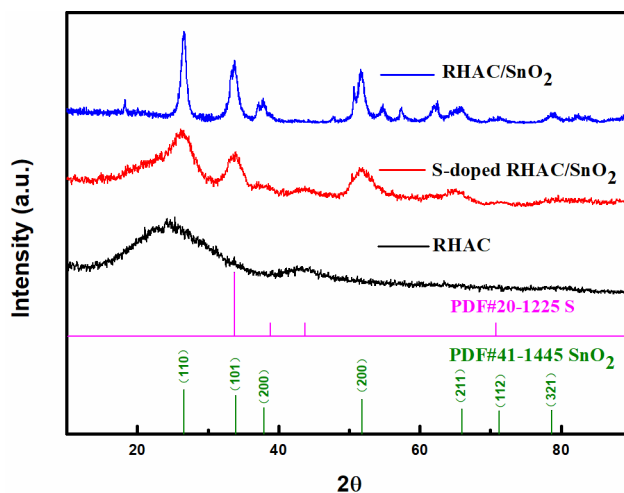
Fig. 1. XRD pattern of RHAC, RHAC/SnO₂, and S doped RHAC/SnO₂
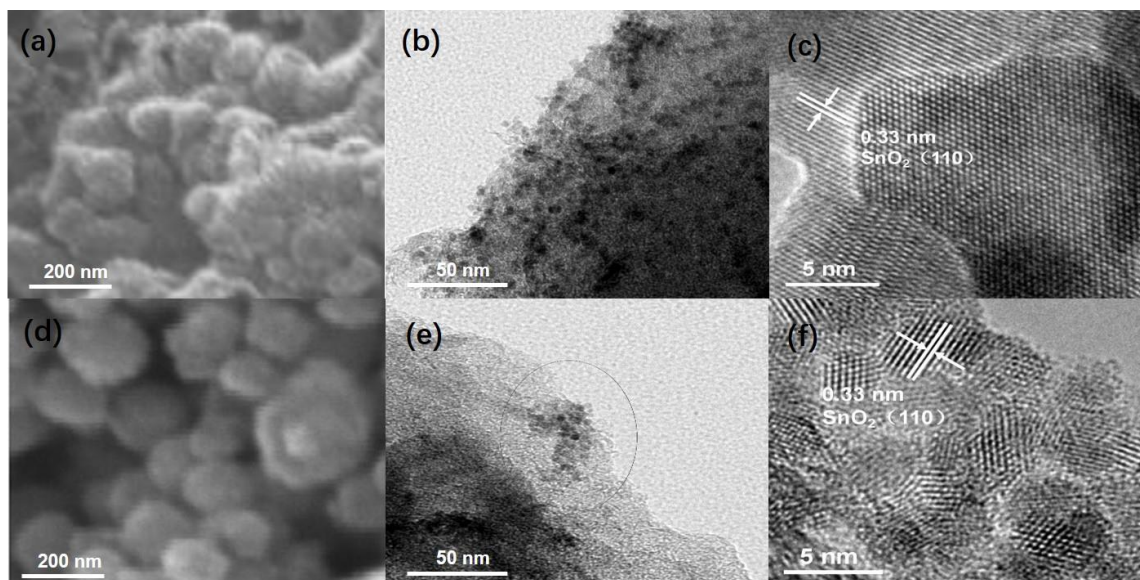
Fig. 2. SEM and TEM of RHAC/SnO$_2$ (a,b,c) and S-doped RHAC/SnO$_2$ (d,e,f)

The morphology of the sample was characterized by scanning electron microscopy and transmission electron microscopy. The SEM and TEM images of RHAC/SnO$_2$ and S-doped RHAC/SnO$_2$ are shown in Fig. 2 (a-c) and (d-f), respectively. Figures 2a and 2d show two surface-like irregular nano particles composite materials that tin oxide uniformly coated on the surface of the porous carbon. As shown in Fig. 2b and Fig. 2e, the spherical particles are assembled from smaller nanoparticles. As shown in Fig. 2c and Fig. 2f, which are TEM (HRTEM) images of the composite, a lattice fringe spacing of 0.33 nm corresponding to the interplanar spacing of (110) of SnO$_2$. The distortion of the lattice fringes further confirmed the low crystallization characteristics of SnO$_2$ in the S-doped RHAC/SnO$_2$ nanocomposites.
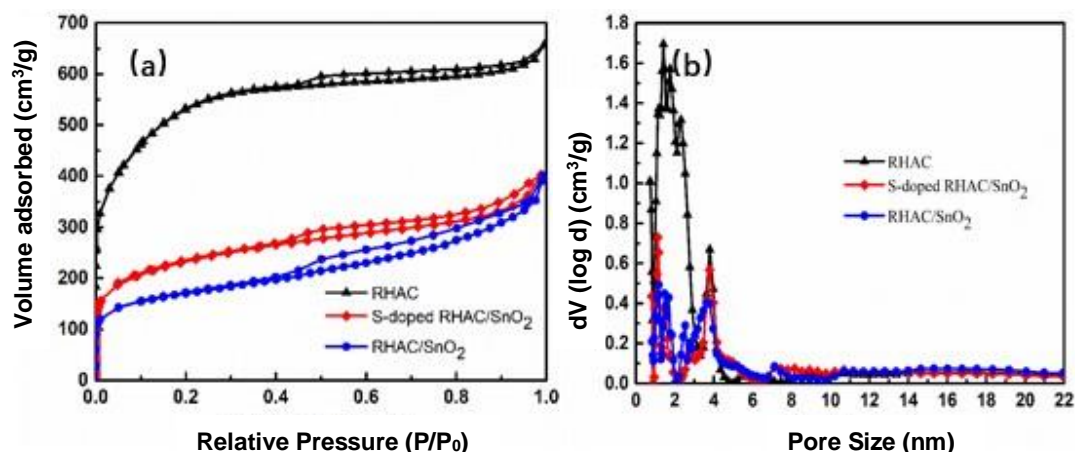
Fig. 3. (a) N$_2$ adsorption/desorption isotherms and (b) Pore size distribution calculated by DFT methods of RHAC, S-doped RHAC/SnO2, RHAC/SnO$_2$

Figure 3 shows the pore structure of RHAC, RHAC/SnO$_2$, and S-doped RHAC/SnO$_2$ composites. The specific surface area, and pore size distribution of porous carbon and its composites were analyzed by N$_2$ adsorption/ desorption isotherm and pore size distribution curves. Figure 3a shows the I + IV isotherm (IUPAC classification) with

high adsorption capacity of RHAC, indicating that the RHAC had abundant micropores and a certain amount of mesopores. When the relative pressure was less than 0.1, the sample adsorption amount rose rapidly, indicating that it had a developed microporous structure. In addition, capillary condensation occurred in the adsorbate, allowing the desorption isotherm to be above the adsorption isotherm, causing adsorption hysteresis. When the relative pressure exceeded 0.95, the adsorption amount rose again rapidly and failed to reach adsorption saturation at a higher partial pressure. Additionally, the adsorption-desorption hysteresis loop appears, showing a type IV isotherm, a representative H4 hysteresis loop, indicating the presence of a certain amount of mesopores (Yue *et al.* 2016).

The composite RHAC/SnO$_2$ and S-doped RHAC/SnO$_2$ have similar pore structure with RHAC. When the relative pressure was less than 0.1, the adsorption amount of the sample increased rapidly. When compared with RHAC, the adsorption amount of decreased, indicating that the micropores of the composite decreased. After SnO$_2$ was loaded on RHAC, it filled most of the micropores in RHAC. As the relative pressure increases, the adsorption and desorption curves of the composites were lower than RHAC, but they still exhibited adsorption and desorption hysteresis loops. This was because after the SnO$_2$ crystal particles were loaded on the RHAC, after filling some of the micropores and mesopores in the RHAC, the specific surface area and pore structure of the composite were greatly reduced, but the mesoporous structure was still preserved. One part of these mesopores were the original mesopores in RHAC that were not filled, and the other part were due to nano tin oxide filling most of the micropores in RHAC and generating mesopores.

The pore size distribution measured by the non-localized density function theory (NLDFT) is shown in Fig.3 b. According to the Brunauer-Emmett-Teller (BET) analysis, the specific surface areas of RHAC, S-doped RHAC/SnO$_2$, and RHAC/SnO$_2$ were 1383, 595, and 478, m$^2 \cdot$g^{-1} respectively. The specific surface area of S-doped RHAC/SnO$_2$ composites were better than those of RHAC/SnO$_2$. It may be that excess thiourea is decomposed into H$_2$S, NH$_3$, CO$_2$, and other gases at high temperature (Dong *et al.* 2011). These gases escape from the composite, resulting in a certain pore structure on the surface of the nano tin oxide. Therefore, this rich porosity S-doped composite is beneficial for the application of supercapacitor electrode materials.
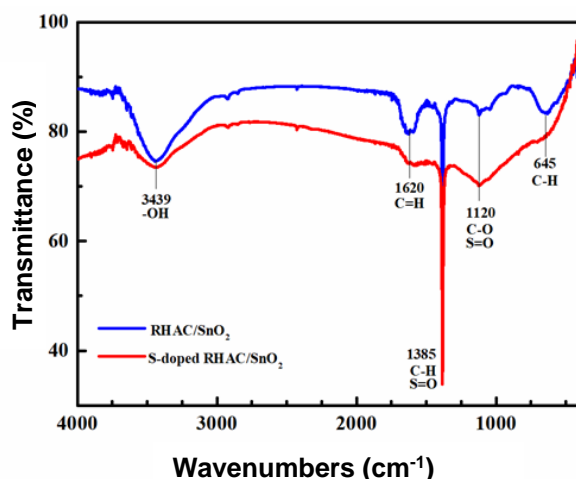
Fig. 4. FTIR of RHAC/SnO$_2$ and S-doped RHAC/SnO$_2$

The composites were characterized by FTIR, as shown in Fig. 4. The peaks of RHAC/SnO$_2$ and S-doped RHAC/SnO$_2$ were mainly at 3493, 1620, 1385, 1120, and 645 cm^{-1}, and functional groups were -OH, C=H, C-H /S=O, C-O /S=O, and C-H, respectively. The peaks of S-doped RHAC/SnO$_2$ at 1385 and 1120 cm^{-1} were stronger than those of RHAC/SnO$_2$, which was an expression of S=O, indicating that S was obviously doped.

X-ray photoelectron spectroscopy (XPS) was used to further evaluate the composition and chemical state of the elements on the surface of RHAC/SnO$_2$ and S-doped RHAC/SnO$_2$ composites. The elemental composition of the composites obtained by XPS analysis is shown in Table 1.

Table 1. Element Composition of Composites Obtained by XPS Analysis

Sample	C (%)	O (%)	Sn (%)	S (%)
RHAC/SnO$_2$	60.44	29.19	10.37	_
S-doped RHAC/SnO$_2$	63.53	22.77	8.63	5.07

Figure 5a shows the XPS test spectrum of two composite materials. The RHAC/SnO$_2$ consisted of three elements: Sn, O, and C, but four elements of Sn, S, O, and C can be observed in S-doped RHAC/SnO$_2$. Both of them showed no significant impurities, which further confirms the formation of composite materials. Figure 5b shows the XPS lines of the Sn 3d elements of the two composites. Both samples showed two peaks at 487.6 and 496 eV, respectively, corresponding to Sn 3d5/2 and Sn 3d3/2. The peak distance between the two peaks is 8.4 eV, and the spin energy separation indicated that both sample surfaces were Sn^{4+} (Wang *et al.* 2015; Yue *et al.* 2016; Gu *et al.* 2017).
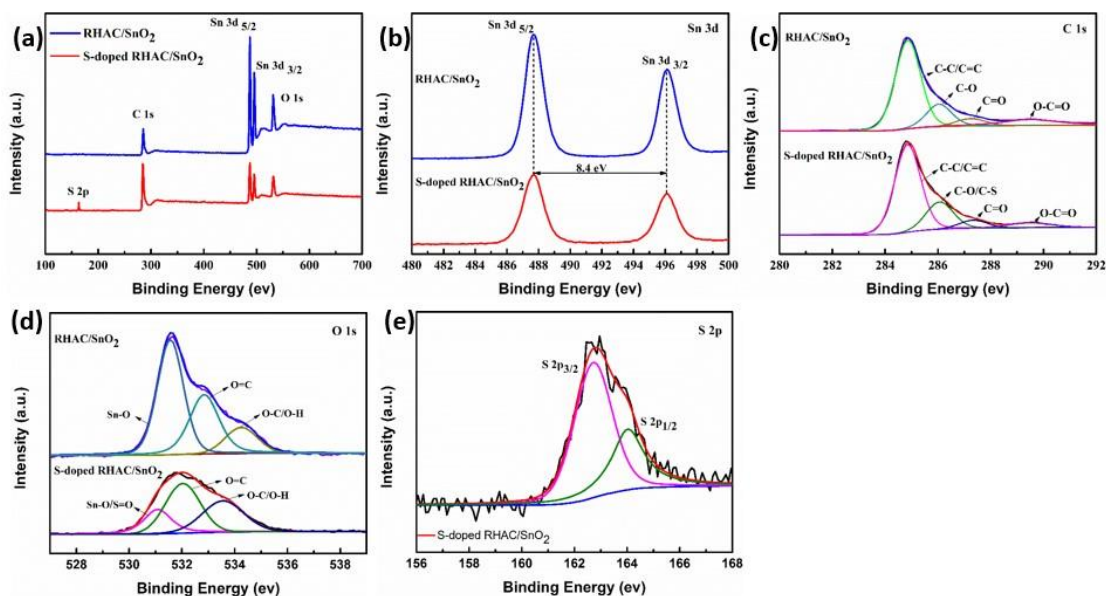
Fig. 5. (a) Survey, (b) Sn 3d region, (c) C 1s region, (d) O 1s region, and (e) S 2p region XPS spectra of S-doped RHAC/SnO$_2$ and RHAC/SnO$_2$

The XPS lines of the C 1s elements of the RHAC/SnO$_2$ and S-doped RHAC/SnO$_2$ samples are shown in Fig. 5c. Each spectrum can be fitted to C-C/C=C (284.8 eV), C-O (286.1 eV), C=O (287.3 eV), and O-C=O (289.5 eV) (Figueiredo *et al.* 1999; Mooss

and Athawale 2016), where the S-doped RHAC/SnO$_2$ sample also had a C-S fit peak at the 286.1 eV position (Bhaskar *et al.* 2014). The XPS line of the C 1s element demonstrates the presence of RHAC in the composite. As shown in Table 2, the relative peak areas of C-C/C=C in the two composite samples were 66.6% and 64%, respectively, and the peak positions were basically the same, indicating that the carbons in the two samples had similar structures.

Figure 5d shows the XPS line of the O 1s element of the RHAC/SnO$_2$ and S-doped RHAC/SnO$_2$ samples. The fitting peak of the O 1s element in the RHAC/SnO$_2$ sample consists of Sn-O (531.5 eV), C=O (532.8 eV) and O-C/O-H (534.2 eV). The fitted peak the O 1s element in the S-doped RHAC/SnO$_2$ sample consists of Sn-O/S=O (531.1 eV), C=O (532 eV) and O-C/O-H (533.5 eV) (Zhou *et al.* 2013b; Bhaskar *et al.* 2014; Yue *et al.* 2016). Due to the doping of S, there is S=O fitting peak at the 531.1 eV position in the S-doped RHAC/SnO$_2$ sample, as shown in Table 3. The C=O and O-C/O-H peaks are derived from RHAC, while the Sn-O peak belongs to SnO$_2$.

Figure 5e shows the XPS line of the S 2p element of the S-doped RHAC/SnO$_2$ sample. The high-resolution S 2p spectrum shows the S 2p double valence at 164 eV and 162.8 eV with a peak spacing of 1.2 eV. Corresponding to the spin orbitals S 2p1/2 and S 2p3/2 (Jönsson *et al.* 2003; Rufford *et al.* 2008; Bhaskar *et al.* 2014), respectively. The introduction of electron-rich S atoms in the carbon material improves the surface environment of the carbon material and increases the polarization and electron conductivity of the surface of the electrode material, which is beneficial to the electrochemical performance of the material. Conversely, S combines with C and O to form a sulfur-containing functional group, which undergoes a redox reaction during charge and discharge to generate a pseudo capacitance and stores more charge by generating a Faraday reaction at these sites, which has a positive effect on capacitance (Wang *et al.* 2014; An *et al.* 2016; Deng *et al.* 2018; Jiang *et al.* 2018; Ji *et al.* 2019).

Table 2. (a) XPS Peak Fitting Results of RHAC/SnO$_2$ and (b) S-doped RHAC/SnO$_2$ in the C1s Region

(a) Peak	Binging energy (eV)	Relative peak area (%)	FWHM (eV)
C-C/C=C	284.8	66.6%	1.15
C-O	286.1	21.6%	1.22
C=O	287.3	6.1%	1.24
O-C=O	289.5	5.7%	1.92
(b) Peak	Binging energy (eV)	Relative peak area (%)	FWHM (eV)
C-C/C=C	284.8	64.0%	1.13
C-O/C-S	286.1	17.1%	1.13
C=O	287.2	6.0%	1.34
O-C=O	289.5	12.9%	2.52

Table 3. (a) XPS Peak Fitting Results of RHAC/SnO$_2$ and (b) S-doped RHAC/SnO$_2$ in O1s Region

(a) Peak	Binging energy (eV)	Relative peak area (%)	FWHM (eV)
Sn-O	531.5	52.7%	1.16
O=C	532.8	33.5%	1.31
O-C/O-H	534.2	13.8%	1.44
(b) Peak	Binging energy (eV)	Relative peak area (%)	FWHM (eV)
Sn-O/S=O	531.1	21.7%	1.22
O=C	532	43.9%	1.55
O-C/O-H	533.5	34.4%	1.85

Electrochemical Properties of RHAC/SnO$_2$ and S-doped RHAC/SnO$_2$

The electrochemical properties of the product were investigated using a three-electrode device. The cyclic voltammetry (CV) curves for RHAC, RHAC/SnO$_2$, and S-doped RHAC/SnO$_2$ at the same scan rate of 20 mV/s are shown in Fig. 6a. The CV curve of RHAC shows no redox peaks, which is a typical electric double layer capacitor. While RHAC/SnO$_2$ and S-doped RHAC/SnO$_2$ exhibited a tiny hump, there was a redox reaction in the electrode material. Compared with pure biochar, the metal oxide SnO$_2$ and S-doped have positive significance to specific capacitance. The integrated area of the CV curve of the RHAC/SnO$_2$ material is smaller than that of the S-doped RHAC/SnO$_2$, indicating that the S-doped composite has a higher specific capacitance. On one hand, due to the low crystallinity of the synthesized tin oxide, the low crystal or amorphous form can achieve faster charge transfer and better than the high crystal phase. More structural defects and disorder bring the better cycle stability (Chen *et al.* 2017; Owusu *et al.* 2017). Alternatively, the introduction of S heteroatoms in composites has a positive effect on the improvement of the capacitance (Tsubota *et al.* 2011; Zhao *et al.* 2012; Seredych *et al.* 2014).

Figure 6b shows the static voltage charge-discharge curves for three samples at a current density of 1.5 A/g. These curves are almost symmetrical during charging and discharging, exhibiting ideal capacitive behavior from the corresponding discharge. The specific capacitances that can be calculated from the discharge curve are 141 F/g, 177 F/g, and 215 F/g, respectively. Although RHAC has excellent rate performance (Wang *et al.* 2018), its capacitance is lower than 170 F/g. The composite material RHAC/SnO$_2$ can provide a high capacitance of 177 F/g at a high current density of 1.5 A/g, and the specific capacitance of S-doped RHAC/SnO$_2$ can reach 215 F/g. It is further demonstrated that the pseudo capacitance induced by the redox reaction can improve the overall capacitance strength of the composite material, so that the charging and discharging time is longer than that of the biomass carbon material, and the composite material doped with S heteroatom has better performance.
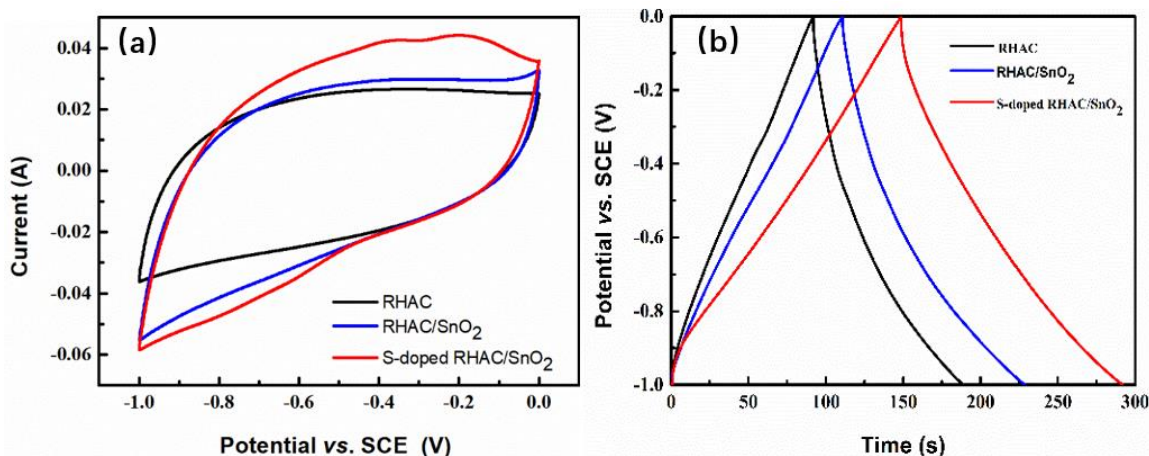
Fig. 6. (a) CV curves at 20 mV/s scan rates and (b) GCD curves at 1.5 A/g current densities of RHAC, RHAC/SnO_2 and S-doped RHAC/SnO_2

Figure 7a shows the CV plot of S-doped RHAC/SnO_2 at the sweep speeds from 20 to 100 mV/s. These CV curves exhibit rectangular shapes at low scanning rates, indicating the charge storage mechanism of the surface of the electrode material. When the scanning rate was increased to 100 mV/s, the rectangular shape could still be maintained, showing a lower electrochemical polarization. Figure 7b shows the charge-discharge curves of S-doped RHAC/SnO_2 composite at different current densities of 0.4, 1, 2, 4, and 8 A/g, which were almost symmetrical during charging and discharging. The ideal capacitive behavior, the small curvature of the charge and discharge curve reflected the pseudo capacitance behavior of the material, consistent with the results of the redox peak appearing in the CV curve.

The specific capacitance values S-doped RHAC/SnO_2 composite at different current densities of 0.4, 1, 2, 4, and 8 A/g are shown in Fig. 7c, which were 283 F/g, 228 F/g, 186 F/g, 176 F/g, and 152 F/g, respectively. When the current density was increased from 0.4 A /g to 4 A /g, the specific capacity of the material still was able to maintain 62.2% of its maximum value with good rate performance. As shown in Fig. 7d, at a current density of 0.4 A/g, after 5000 cycles of charge and discharge, the specific capacitance is maintained at about 78.5%, indicating that this S-doped RHAC/SnO_2 composite material electrode has a long cycle life, which is better than the 70% specific capacitance retention rate of RHAC/SnO_2.
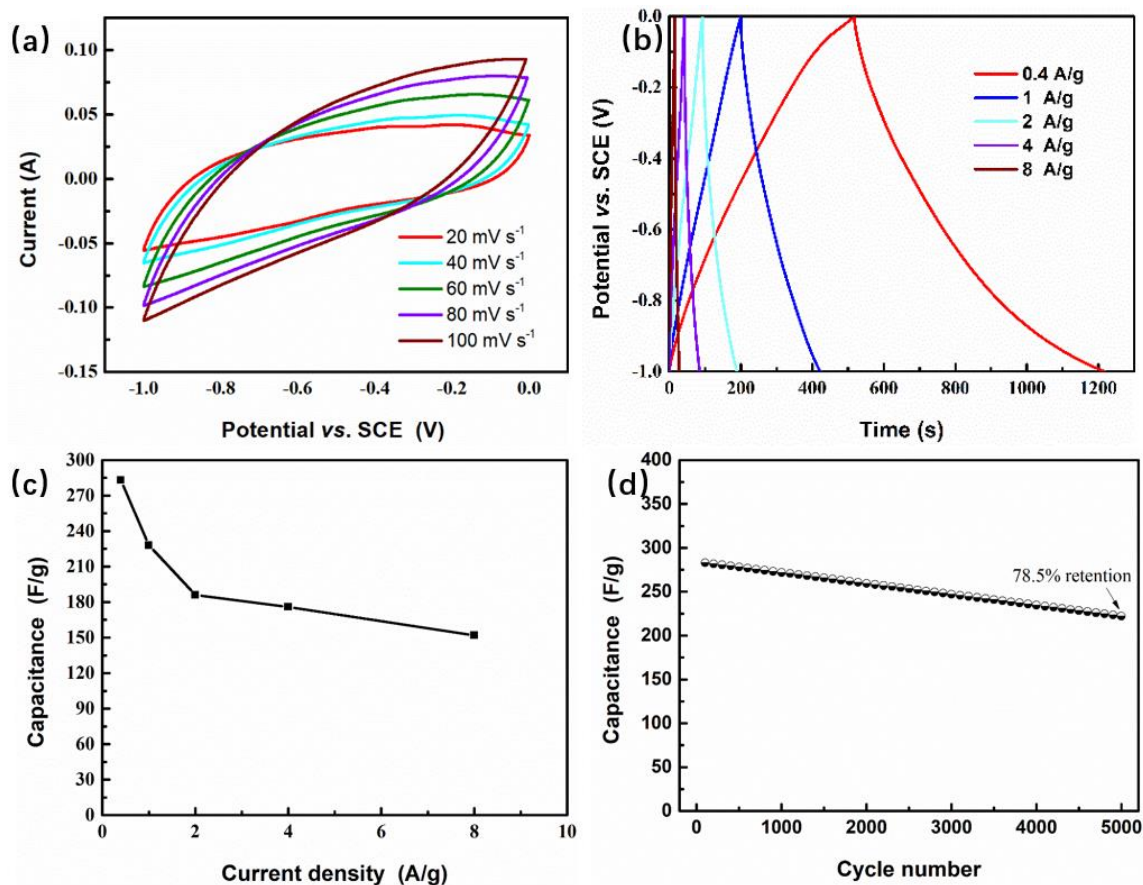
Fig. 7. (a) CV curves at scan rates from 20 to 100 mV/s, (b) GCD curves at current densities from 0.4 to 8 A/g, (c) Specific capacitance at different current densities and (d) Cycling performance at current density at 0.4 A/g of S-doped RHAC/SnO₂

Figure 8 shows the Nyquist curves for the RHAC, S-doped RHAC/SnO₂, and RHAC/SnO₂ electrode materials. In the high frequency region, the intersection of the curve and the horizontal axis of the coordinate is the equivalent series resistance (R_s) of the material, and R_s includes the resistance of the electrode, the ionic resistance of the electrolyte, and the contact resistance of the active material and the collector interface. The lower the R_s value, the higher the electronic conductivity. The R_s of the three materials are all low, about 0.5, indicating that the porous carbon RHAC and its composites have good electronic conductivity. In the intermediate frequency region, the diameter of the arc corresponds to the charge transfer resistance (R_{ct}), and the arcs diameters of the RHAC, S-doped RHAC/SnO₂, and RHAC/SnO₂ increase sequentially, indicating that the ion transport and electron conduction properties of the material surface are sequentially weakened. RHAC has faster adsorption/desorption at the electrode surface.

The impedance curve in the low frequency region was linear, indicating the resistance of the electrolyte ions to the electrochemically active sites inside the electrode material, and the Warburg impedance (W), the small slope of the oblique line indicates that the electrolyte ions diffuse to the active site surface at a lower rate. By comparison, it was found that RHAC porous carbon material had abundant mesopores and macropores. This situation favored the diffusion of ions inside the electrode material, so the linear

slope was the largest. After RHAC was loaded with tin oxide, some of the pores were filled with tin oxide crystal particles, and the pores were filled. This reduces the diffusion speed of ions inside the material, so that the linear slope of the low frequency region decreases. The S-doped $RHAC/SnO_2$ composite material had lower crystallinity and higher specific surface area than the undoped composite material, so the linear slope of the low frequency region was high and close to RHAC.
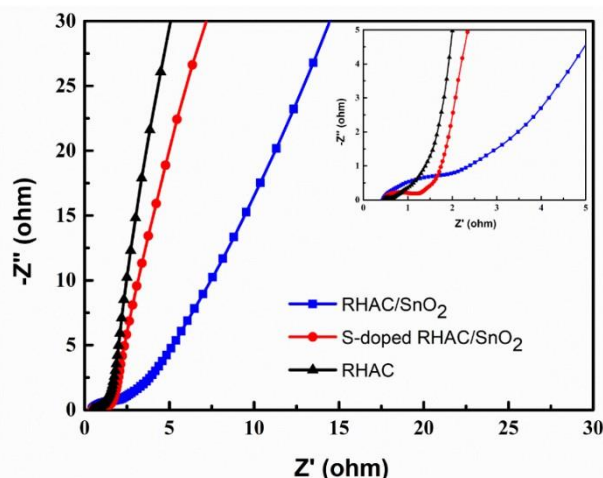
Fig. 8. Nyquist plots of RHAC, S-doped $RHAC/SnO_2$ and $RHAC/SnO_2$ electrodes

CONCLUSIONS

1. Synthetic heterostructured nanocomposites with highly conductive porous matrix, large surface area, and short ion/electron transport paths showed enhanced pseudo capacitance kinetics, and composite specific capacitance properties were improved over biomass porous materials. In terms of specific surface area, surface polarity, and active sites for participation in the Faraday reaction, the S-doped $RHAC/SnO_2$ electrode materials were superior to the $RHAC/SnO_2$ electrode materials. The doped S atom combined with the C and O atoms in the material to form a new functional group, which participated in the reaction of the pseudocapacitor, so that the specific capacitance of the material increased.

2. The specific capacitances of RHAC, $RHAC/SnO_2$, and S-doped $RHAC/SnO_2$ electrode materials were 141 F/g, 177 F/g, 215 F/g at a high current density of 1.5 A/g. The specific capacitance of S-doped $RHAC/SnO_2$ composite at different current densities of 0.4, 1, 2, 4, and 8 A/g were 283 F/g, 228 F/g, 186 F/g, 176 F/g, and 152 F/g respectively.

3. The current density is increased from 0.4 A/g to 4 A/g, and the specific capacity of the S-doped $RHAC/SnO_2$ composite could be maintained at 62.2% of its maximum value with good rate performance. At a current density of 0.4 A/g, the charge capacity was maintained at about 78.5% after 5000 cycles of charge and discharge, indicating that the electrode has a long cycle life.

4. The nanostructured metal oxides loaded on gasified rice husk carbon based porous carbon, providing an example for efficient and cost effective supercapacitor electrode materials.

ACKNOWLEDGEMENTS

REFERENCES CITED

An, G., Lee, D., Lee, Y., and Ahn, H. (2016), "Ultrafast lithium storage using antimony-doped tin oxide nanoparticles sandwiched between carbon nanofibers and a carbon skin," *ACS Applied Materials & Interfaces* 8(44), 30264-30270. DOI: 10.1021/acsami.6b10868

Bhaskar, A., Deepa, M., Ramakrishna, M., and Rao, T. N. (2014), "Poly(3,4-ethylenedioxythiophene) sheath over an SnO_2 hollow spheres/graphene oxide hybrid for a durable anode in Li-ion batteries" *The Journal of Physical Chemistry C* 118, 7296-7306. DOI: 10.1021/jp412038y

Chen, J., Zhou, X., Mei, C., Xu, J., Zhou, S., and Wong, C. (2017). "Evaluating biomass-derived hierarchically porous carbon as the positive electrode material for hybrid Na-ion capacitors," *Journal of Power Sources* 342, 48-55. DOI: 10.1016/j.jpowsour.2016.12.034

Chuanxiang, Z., Yuming, D., Xiancong, H., Zhixin, B., and Hengzhi, Z. (2016). "Micro-wave-assisted synthesis of NiO/C and its capacitance property," *Rare Metal Materials and Engineering* 45(5), 1093-1099. DOI: 10.1016/S1875-5372(16)30100-X

Deng, C., Liu, Y., Lu, Z., Ma, C., Ge, T., Li, W., and Yang, G. (2018). "The effect of passivation film in preparation 3D structural carbon paper/tin oxide@carbon as freestanding anode for lithium-ion batteries," *Applied Surface Science* 435(30), 1307-1313. DOI: 10.1016/j.apsusc.2017.11.275

Deosarkar, M. P., Pawar, S. M., Sonawane, S. H., and Bhanvase, B. A. (2013). "Process intensification of uniform loading of SnO_2 nanoparticles on graphene oxide nanosheets using a novel ultrasound assisted in situ chemical precipitation method," *Chemical Engineering and Processing: Process Intensification* 70, 48-54. DOI: 10.1016/j.cep.2013.05.008

Dong, W., Wang, X., Li, B., Wang, L., Chen, B., Li, C., Li, X., Zhang, T. and Shi, Z. (2011). "Hydrothermal synthesis and structure evolution of hierarchical cobalt sulfide nanostructures," *Dalton Transactions*, 40(1), 243-248. DOI: 10.1039/C0DT01107J

Figueiredo, J. L., Pereira, M. F. R., Freitas, M. M. A., and Órfão, J. J. M. (1999). "Modification of the surface chemistry of activated carbons," *Carbon* 37(9), 1379-1389. DOI: 10.1016/S0008-6223(98)00333-9

Gu, Y., Jiao, Z., Wu, M., Luo, B., Lei, Y., Wang, Y., Wang, L., and Zhang, H. (2017). "Construction of point-line-plane (0-1-2 dimensional) Fe_2O_3-SnO_2/graphene hybrids as the anodes with excellent lithium storage capability," *Nano Research* 10(1), 121-133. DOI: 10.1007/s12274-016-1271-y

He, X., Ling, P., Qiu, J., Yu, M., Zhang, X., Yu, C., and Zheng, M. (2013). "Efficient preparation of biomass-based mesoporous carbons for supercapacitors with both high energy density and high power density," *Journal of Power Sources* 240, 109-113. DOI: 10.1016/j.jpowsour.2013.03.174

Huang, P., Lethien, C., Pinaud, S., Brousse, K., Laloo, R., Turq, V., Respaud, M., Demortière, A., Daffos, B., Taberna, P.L., Chaudret, B., Gogotsi, Y., and Simon, P., (2016). "On-chip and freestanding elastic carbon films for micro-supercapacitors," *Science* 351(6274), 691-695. DOI: 10.1126/science.aad3345

Hwang, S., and Hyun, S. (2007). "Synthesis and characterization of tin oxide/carbon aerogel composite electrodes for electrochemical supercapacitors," *Journal of Power Sources* 172(1), 451-459. DOI: 10.1016/j.jpowsour.2007.07.061

Ji, H., Ma, C., Ding, J., Yang, J., Yang, G., Chao, Y., and Yang, Y. (2019). "Complementary stabilization by core/sheath carbon nanofibers/spongy carbon on submicron tin oxide particles as anode for lithium-ion batteries," *Journal of Power Sources* 413, 42-49. DOI: 10.1016/j.jpowsour.2018.12.022

Jiang, J., Ma, C., Yang, Y., Ding, J., Ji, H., Shi, S., and Yang, G. (2018). "Synergetic interface between NiO/Ni_3S_2 nanosheets and carbon nanofiber as binder-free anode for highly reversible lithium storage," *Applied Surface Science* 441, 232-238. DOI: 10.1016/j.apsusc.2018.02.053

Jiang, Y., Yuan, T., Sun, W., and Yan, M. (2012). "Electrostatic spray deposition of porous SnO_2/Graphene anode films and their enhanced lithium-storage properties," *ACS Applied Materials & Interfaces* 4, 6216-6220. DOI:10.1021/am301788m

Jin, Y., Min, K., Seo, S., Shim, H., and Kim, D. (2011). "Enhanced Li storage capacity in 3 nm diameter SnO_2 nanocrystals firmly anchored on multiwalled carbon nanotubes," *The Journal of Physical Chemistry C* 115(44), 22062-22067. DOI: 10.1021/jp208021w

Jönsson, S. K. M., Birgerson, J., Crispin, X., Greczynski, G., Osikowicz, W., Denier Van Der Gon, A.W., Salaneck, W. R., and Fahlman, M. (2003). "The effects of solvents on the morphology and sheet resistance in poly(3,4-ethylenedioxythiophene)-polystyrenesulfonic acid (PEDOT-PSS) films," *Synthetic Metals* 139(1), 1-10. DOI: 10.1016/S0379-6779(02)01259-6

Joshi, B. N., An, S., Jo, H. S., Song, K. Y., Park, H. G., Hwang, S., Al-Deyab, S. S., Yoon, W. Y., and Yoon, S. S., (2016). "Flexible, freestanding, and binder-free SnO_x–ZnO/carbon nanofiber composites for lithium ion battery anodes," *ACS Applied Materials & Interfaces* 8(14), 9446-9453. DOI: 10.1021/acsami.6b01093

Kim, H., Cook, J. B., Lin, H., Ko, J. S., Tolbert, S. H., Ozolins, V., and Dunn, B. (2016). "Oxygen vacancies enhance pseudocapacitive charge storage properties of $MoO_3−x$," *Nature Materials* 16, 454-460. DOI: 10.1038/nmat4810

Lang, X. Y., Yuan, H. T., Iwasa, Y., Chen, M. W. (2011). "Three-dimensional nanoporous gold for electrochemical supercapacitors," *Scripta Materialia* 64(9), 923-926. DOI: 10.1016/j.scriptamat.2011.01.038

Li, Z. J., Chang, T. X., Yun, G. Q., and Jia, Y. (2012). "Coating single walled carbon nanotube with SnO_2 and its electrochemical properties," *Powder Technology* 224, 306-310. DOI: 10.1016/j.powtec.2012.03.012

Lim, A., Shim, H., Seo, S., Lee, G., Park, K., and Kim, D. (2012). "Biomineralized Sn-based multiphasic nanostructures for Li-ion battery electrodes," *Nanoscale* 4(15), 4694-4701. DOI: 10.1039/C2NR31056B

Lim, S. P., Huang, N. M., and Lim, H. N. (2013). "Solvothermal synthesis of SnO_2/graphene nanocomposites for supercapacitor application," *Ceramics International* 39(6), 6647-6655. DOI: 10.1016/j.ceramint.2013.01.102

Ma, C., Zhang, W., He, Y., Gong, Q., Che, H., and Ma, Z. (2016). "Carbon coated SnO_2 nanoparticles anchored on CNT as a superior anode material for lithium-ion

batteries," *Nanoscale* 8(7), 4121-4126. DOI: 10.1039/C5NR07996A

Madian, M., Klose, M., Jaumann, T., Gebert, A., Oswald, S., Ismail, N., Eychmüller, A., Eckert, J., and Giebeler, L. (2016). "Anodically fabricated TiO_2–SnO_2 nanotubes and their application in lithium ion batteries," *Journal of Materials Chemistry A* 4, 5542-5552. DOI: 10.1039/C6TA00182C

Mooss, V. A., and Athawale, A. A. (2016). "Polyaniline-graphene oxide nanocomposites: Influence of nonconducting graphene oxide on the conductivity and oxidation-reduction mechanism of polyaniline," *Journal of Polymer Science Part A: Polymer Chemistry* 54(30), 3778-3786. DOI: 10.1002/pola.28277

Mu, J., Chen, B., Guo, Z., Zhang, M., Zhang, Z., Shao, C., and Liu, Y. (2011). "Tin oxide (SnO_2) nanoparticles/electrospun carbon nanofibers (CNFs) heterostructures: Controlled fabrication and high capacitive behavior," *Journal of Colloid and Interface Science* 356(2), 706-712. DOI: 10.1016/j.jcis.2011.01.032

Owusu, K. A., Qu, L., Li, J., Wang, Z., Zhao, K., Yang, C., Hercule, K. M., Lin, C., Shi, C., Wei, Q., Zhou, L., and Mai, L. (2017). "Low-crystalline iron oxide hydroxide nanoparticle anode for high-performance supercapacitors," *Nature Communications* 8(14264). DOI: 10.1038/ncomms14264

Peng, H., Li, R., Hu, J., Deng, W., and Pan, F. (2016). Core-Shell Sn-Ni-Cu-Alloy@Carbon nanorods to array as three-dimensional anode by nanoelectrodeposition for high-performance lithium ion batteries," *ACS Applied Materials & Interfaces* 8(19), 12221-12227. DOI: 10.1021/acsami.6b03383

Rakhi, R. B., Chen, W., Cha, D., and Alshareef, H. N. (2012). "Substrate dependent self-organization of mesoporous cobalt oxide nanowires with remarkable pseudocapacitance. *Nano Letters* 12(5), 2559-2567. DOI:10.1021/nl300779a

Rufford, T. E., Hulicova-Jurcakova, D., Zhu, Z., and Lu, G. Q. (2008). "Nanoporous carbon electrode from waste coffee beans for high performance supercapacitors," *Electrochemistry Communications* 10(10), 1594-1597. DOI: 10.1016/j.elecom.2008.08.022

Seredych, M., Singh, K., and Bandosz, T. J. (2014). "Insight into the capacitive performance of sulfur-doped nanoporous carbons modified by addition of graphene phase," *Electroanalysis* 26(1), 109-120. DOI: 10.1002/elan.201300161

Tang, W., Zhang, Y., Zhong, Y., Shen, T., Wang, X., Xia, X., and Tu, J. (2017). "Natural biomass-derived carbons for electrochemical energy storage," *Materials Research Bulletin*, 88, 234-241. DOI: 10.1016/j.materresbull.2016.12.025

Tsubota, T., Takenaka, K., Murakami, N., Ohno, T. (2011). "Performance of nitrogen- and sulfur-containing carbon material derived from thiourea and formaldehyde as electrochemical capacitor," *Journal of Power Sources* 196(23), 10455-10460. DOI: 10.1016/j.jpowsour.2011.07.025

Wang, F., Chen, L., Deng, C., Ye, H., Jiang, X., and Yang, G. (2014). "Porous tin film synthesized by electrodeposition and the electrochemical performance for lithium-ion batteries," *Electrochimica Acta* 149, 330-336. DOI: 10.1016/j.electacta.2014.10.074

Wang, H., and Rogach, A. L. (2014). "Hierarchical SnO_2 nanostructures: Recent advances in design, synthesis, and applications. *Chemistry of Materials* 26, 123-133. DOI:10.1021/cm4018248

Wang, H., Wu, D., Zhou, J., Ma, H., Xu, D., Qian, B., Tao, S., and Wang, Z. (2018). "Preparation of supercapacitor electrode from gasified rice husk carbon," *BioResources* 13(2). DOI: 10.15376/biores.13.2.4279-4289

Wang, X., Wang, Y., Tian, F., Liang, H., Wang, K., Zhao, X., Lu, Z., Jiang, K., Yang, L.,

and Lou, X. (2015). "From the surface reaction control to gas-diffusion Control: The synthesis of hierarchical porous SnO_2 microspheres and their gas-sensing mechanism," *The Journal of Physical Chemistry C* 119(28), 15963-15976. DOI: 10.1021/acs.jpcc.5b01397

Xia, L., Wang, S., Liu, G., Ding, L., Li, D., Wang, H., and Qiao, S. (2016). "Flexible SnO_2/N-doped carbon nanofiber films as integrated electrodes for lithium-ion batteries with superior rate capacity and long cycle life," *Small* 12(7), 853-859. DOI: 10.1002/smll.201503315

Yue, L., Xue, C., Huang, B., Xu, N., Guan, R., Zhang, Q., and Zhang, W. (2016). "High performance hollow carbon@SnO2@graphene composite based on internal-external double protection strategy for lithium ion battery," *Electrochimica Acta* 220, 222-230. DOI: 10.1016/j.electacta.2016.10.110

Zhao, X., Zhang, Q., Chen, C., Zhang, B., Reiche, S., Wang, A., Zhang, T., Schlögl, R., and Su, D. S. (2012). "Aromatic sulfide, sulfoxide, and sulfone mediated mesoporous carbon monolith for use in supercapacitor," *Nano Energy* 1, 624-630. DOI: 10.1016/j.nanoen.2012.04.003

Zhou, C., Zhang, Y., Li, Y., and Liu, J. (2013a). "Construction of high-capacitance 3D CoO@polypyrrole nanowire array electrode for aqueous asymmetric supercapacitor," *Nano Letters* 13, 2078-2085. DOI:10.1021/nl400378j

Zhou, G., Wang, D., Li, L., Li, N., Li, F., and Cheng, H. (2013b). "Nanosize SnO_2 confined in the porous shells of carbon cages for kinetically efficient and long-term lithium storage," *Nanoscale* 5, 1576-1582. DOI: 10.1039/C2NR33482H

Zhou, Y., Wang, Y., Wang, J., Lin, L., Wu, X., and He, D. (2018). "Controlled synthesis and characterization of hybrid Sn-doped Co_3O_4 nanowires for supercapacitors," *Materials Letters* 216, 248-251. DOI: 10.1016/j.matlet.2018.01.047